Revision 1

Interstratification of graphene-like carbon layers within black talc from Southeastern China: Implications to sedimentary talc formation

Chengxiang Li [a, b], Rucheng Wang [a,*], Huifang Xu [b,*], Xiancai Lu [a], Hiromi Konishi [b, c], and Kun He[d]

[a] State Key Laboratory for Mineral Deposits Research, School of Earth Sciences and Engineering, Nanjing University, Nanjing 210093, China

[b] NASA Astrobiology Institute, Department of Geoscience, University of Wisconsin-Madison, 1215 West Dayton Street, Madison WI 53706, USA

[c] Department of Geology, Niigata University, 8050 Ikarashi 2-cho, Nishi-ku, Niigata 950-2181, Japan

[d] State Key Laboratory for Enhanced Oil Recovery, Beijing 10083, China

*: Corresponding authors: rcwang@nju.edu.cn; hfxu@geology.wisc.edu

Abstract Large deposits of unusual black talc interstratified with dolostone layers of the late Neoproterozoic Dengying Formation were discovered in Guangfeng County, Jiangxi Province, southeastern China. The black talc ore exhibits primarily oolitic structures and consists mainly of talc (30–70 wt%), dolomite, and quartz, with trace amounts of pyrite and apatite. The ooids are composed of nearly pure black talc crystals, most of which consist of ultrafine nano-plates. The black talc contains small amounts of carbon, which causes the black coloring. Raman spectra and X-ray photoelectron spectroscopy (XPS) results indicate structural disorder and chemical impurities within bonds (e.g., sp^3 hybridized carbon and C–O bonds) in the carbonaceous material, instead of perfectly structured graphite or graphene. Isolated graphene-like carbon interlayers are present in the talc nano-crystals, as shown by Z-contrast transmission electron microscope (TEM) imaging. Based on previous studies on Mg-silicate precipitation from surface water, we propose a sedimentary formation mechanism for the black talc, in which tetrahedral–octahedral–tetrahedral (T–O–T) layers of Mg-silicates, 1~2 unit cells thick, co-precipitated with abundant organic matter derived from microorganisms thriving in locally Al-depleted sea water with high concentrations of Mg^{2+} and SiO_2 (aq), in a shallow marine or lagoonal environment. The involvement of organic matter may have facilitated the precipitation of Mg-silicate. Further diagenesis and re-crystalliztion of the biomass-coated precursor resulted in the formation of graphene-like layers between neighboring talc nano-crystals with same orientation.

Key words: black talc, graphene-like carbon, interstratification structure, sedimentary talc

1. Introduction

Clay minerals are common components of altered mafic and ultramafic rocks, sediments, and soils, and they form through processes such as authigenesis, diagenesis, weathering, and hydrothermal alteration (Bergaya and Lagaly 2013). Structurally, clay minerals consist basically of tetrahedral (T) sheets composed of tetrahedra (with Si^{4+}, Al^{3+}, or Fe^{3+} in the tetrahedral centers) and octahedral (O) sheets composed of octahedra (with Al^{3+}, Mg^{2+}, Fe^{3+}, Fe^{2+}, or other cations in the octahedral centers), which are stacked in different ways with or without interlayer cations (e.g., kaolinite is a 1:1 or T–O type clay mineral with octahedra occupied by Al). Talc is a 2:1 (T–O–T) type clay mineral without interlayer cations that possesses the ideal chemical formula of $Mg_3Si_4O_{10}(OH)_2$, and which shows very limited substitution of Al^{3+} or Fe^{3+} for Mg^{2+} (Rayner and Brown 1973; Bergaya and Lagaly 2013). Talc is normally white, grey or pale green in color and has a hardness of 1 on the Mohs' hardness scale. The structure of talc is relatively simple and stable, with few variations and therefore, the mineral exhibits fewer potential space for modifications than other 2:1 type clay minerals, such as smectite. Nonetheless, the discovery of the large black talc deposits in southern China, with estimated reserves of more than a half billion tons, has drawn attention on account of its huge reserves, unusual color, unique environment of formation and potential for industrial applications (Fan 1990; Di 1993; Lei et al. 2012; Li et al. 2013).

The black talc deposits in Guangfeng County occur in the late Neoproterozoic

Dengying Formation. The black talc ores occur in stratiform, stratoid, or lentoid shapes, and display primary oolitic structures. Some pisolitic or schistose ores, which are present in the cores of folds or near faults, are considered to be the results of dynamically transformed oolitic ores. The oolitic black talc ores consist mainly of black talc ooids that are cemented by micro-crystals of dolomite and quartz, with minor pyrite and apatite (Li et al. 2013).

Early studies on the black talc showed that the unusual black color of the talc at Guangfeng is due to the presence of carbonaceous matter (CM) (Fan 1990; Di 1993; Li et al. 2013), although the exact origin of the color has not been recognized. Our previous study roughly demonstrates the mineralogical characteristics and physicochemical properties of the black talc ores by utilizing multiple mineralogical analysis methods (Li et al. 2013). Nevertheless, the characteristics of the CM and its relationship to the talc crystals remain undefined.

In this study, carbon-related material characterizing methods including Raman spectroscopy and X-ray photoelectron spectroscopy (XPS) were applied to obtain structural information about the contained CM. Scanning transmission electron microscopy (STEM) was used to observe the distribution of CM in the black talc, because of its ability to distinguish different atoms of different atomic numbers through signal intensity variations in Z-contrast images (Kirkland 1998; Nellist 2007; Xu et al. 2014). Carbon isotopic compositions of organic carbon were obtained through pyrolysis–gas chromatography–mass spectrometer analysis in order to trace the origin of CM.

2. Materials and Methods

The black talc samples were collected from a black talc mining quarry (GPS coordinates: N 28°31′22.2″; E 118°15′10.2″) in Guangfeng County, Jiangxi Province, China. Oolitic samples were selected as the representative ones that still preserve primary structural and genetic information of the black talc, as previous studies have shown that the schistose black talc is transformed from the oolitic black talc.

The petrological characteristics of black talc were observed under a polarizing optical microscope. To obtain images of the micromorphology of the black talc, samples were coated with Au and then examined using a JEOL JSM-6490 scanning electron microscope (SEM) coupled with an energy dispersive spectroscopy (EDS) device (Oxford INCA), at an accelerating voltage of 20 kV.

Small black ooids were hand-picked from the crushed oolitic samples, and loaded onto the tip of a glass fiber for X-ray diffraction (XRD) analysis, performed on a Rigaku Rapid II X-ray diffraction system with a 2-D image-plate detector to collect diffraction data, and using a Mo target X-ray source (Mo Kα = 0.71073 Å). The operating conditions were an acceleration voltage of 50 kV and a current of 50 mA. The 2-D images acquired from the 2-D image-plate detector were converted into traditional XRD patterns of 2θ vs. intensity using Rigaku 2DP software. Two additional pure white talc samples were also tested for comparison with the black talc samples, following the same experimental procedures and conditions. One white talc sample consisted of aggregates of fine talc crystals from Trimouns, France, and the other was a well-crystallized monocrystal from Greiner, Tyrol, Austria.

The Raman spectra were acquired from polished flat surfaces of black talc samples, using a Reinishaw inVia Raman spectroscope. The wavelength of the laser was 633 nm and power was kept low at 1.0 mW to avoid laser-induced heating. The spectra were recorded over the range of 100–4000 cm^{-1} with one acquisition per 10 s of accumulations. The position, intensity, and full width at half-maximum (FWHM) of the Raman peaks were obtained by fitting the spectra with a Voigt function after subtracting the linear background. X-ray photoelectron spectroscopy (XPS) analysis was performed on a PHI5000 VersaProbe high performance electron spectrometer, using the monochromatized excitation source of Al Kα (1486.6 eV). All binding energies were referenced to the the C 1s peak at 284.4 eV. The experimental errors were within ±0.1 eV. One entire spectrum of binding energy (0–1330 eV) was acquired, and a specific spectrum of the binding energy interval (280–300 eV) was recorded for the C 1s region to focus on the chemical bond structures of CM in the black talc.

The contents of CM in the black talc samples were too low for direct ^{13}C measurements; therefore, the samples were ground to powder and loaded into sealed gold capsules filled with deionized water, and then subjected to hydrous pyrolysis for 5 days at a temperature of 400 °C and a pressure of 25 MPa. The gas products (water and alkanes with varying numbers of carbon atoms; e.g., CH_4, C_2H_6, and C_3H_8) were collected using a custom-made device connected to a vacuum pump (Zhang et al. 2013). The stable carbon isotopes of the hydrocarbon gases were determined using an

Isochrom II GC–IRMS coupled with a Poraplot Q column. Helium was used as the carrier gas. The heating program was as follows: an initial temperature of 30 °C (isothermal for 3 min), followed by heating at 15 °C/min to 150 °C, and then held isothermal for 8 min. Each measurement was repeated three times to ensure that the errors were <0.5‰.

The samples for TEM and STEM analyses were prepared via Ar^+ ion milling using a Fischione 1010 ion milling machine, performed after the black talc grains had been thinned to <20 μm and mounted on molybdenum TEM grids. The high-resolution TEM (HRTEM) and STEM images were obtained using a spherical aberration-corrected field emission gun (FEG)–STEM (Titan 80-200) operated at 200 kV. For STEM, both bright field (BF) and high-angle annular dark-field (HAADF) images were acquired by utilizing different detectors that collected low-angle coherently scattered electrons and high-angle incoherently scattered electrons, respectively (Kirkland 1998; Nellist 2007). The signal intensity of HAADF imaging (or called Z-contrast imaging) is relative to atomic number ($\sim Z^2$) and number of atoms along the beam direction (Xu et al. 2014).

3. Results

3.1 Mineralogy of black talc

3.1.1 Field observations and analyses of thin section

The Guangfeng black talc ores are present in the upper Sinian Dengying Formation, which overlays upon the Doushantuo Formation that ended deposition at

551 Ma, and which is overlain by the early Cambrian Hetang Formtion at the Ediacaran–Cambrian boundary (~542 Ma) (Ling et al. 2013). The Dengying Formation in the Guangfeng area is mainly composed of gray to dark-gray oolitic or striped siliceous rocks, carbonized siliceous rocks, black talcose rocks that form the black talc deposits, and light gray to gray-white oolitic (or pisolitic) siliceous rocks from the bottom up (Li et al. 2013), which is considered to be formed through deposition of siliceous rocks, Mg-carbonates, Mg-silicates, phosphates, and pyrites, along with organic matter in a shallow marine environment (Fan 1990; Di 1993; Li 1997; Liu 2008; Lei et al. 2012).

The black talc ore bodies extend intermittently over long distances (kilometers) along the northeast direction at different scales (meters to dozens of meters thick) and are distributed as layered or lentoid shapes in the open field (Li et al. 2013); they are surrounded by black siliceous and siliceous carbonate rocks (Fig. 1a). The ore bodies show honeycomb structures consisting of black irregular spherical granules (approximately millimeter-sized) in white or grey cement (Fig. 1b). Near faults and folds, the ore bodies tend to exhibit schistose structure induced by structural activities.

Under plane-polarized light, the black talc granules are light brown in color, which is significantly different from the colorless transparent white talc of varying origins (Fig. 1c). Under crossed-polarized light, remarkable concentric structures are observed caused by non-uniform extinction inside granules (Fig. 1d), which is a typical characteristics of oolitic textures in sedimentary rocks. The cement is composed of micro-crystals of dolomite and quartz with irregular anhedral shapes.

3.1.2 Micromorphology of black talc: SEM and HRTEM observations

Scanning electron microscope images show that the black talc ooids are assemblages of submicron-sized talc flakes, which are actually nano-plates of talc (Fig. 2a and b). In some areas, extremely tiny talc plates (1–2 μm in size) are surrounded by much smaller talc flakes (Fig. 2c).

The nanoscale size of the black talc crystals was further verified in HRTEM images, which show that in the ***c*** direction, the black talc crystals are several tens of nanometers thick, while in the *(00l)* plane, their maximum diameters are one hundred to hundreds of nanometers. Perfect lamellar structures of talc crystals are observed when the electron beam is parallel or nearly parallel to the *(00l)* face of the talc crystals (Fig. 2d). Fast Fourier transform (FFT) patterns of the lamellar areas display bright and sharp (*00l*) reflections, showing periodic repetition of T–O–T layers in the talc crystals. However, the spots that represent (*11l*) reflections are streaking along ***c*** direction, indicating the rotational stacking disorder of T–O–T layers along ***c***-axis (Fig. 2e).

3.1.3 Crystal structure of bulk black talc: XRD analysis

The XRD analysis confirmed that the ooids (black talc, Fig. 3a) consist of pure talc crystals; the analysis detected no quartz or dolomite peaks. The XRD pattern shows a relatively sharp (*001)* peak at a d value of 9.435 Å, while the peaks of the (*020)* and *(110)* planes are asymmetrical and tail off to high angles, which is caused by disordered stacking of T–O–T layers (Fig. 2e).The crystals do not show sharp *(02l)* or *(11l)* peaks on account of disordered stacking. Similar patterns were acquired as well for metamorphic white talc sample from Trimouns, France (sample WT-1, Fig. 3a), indicating their resemblance on the relatively poor crystallinity. However, for the well-crystallized white talc (sample WT-2, Fig. 3a), the XRD analysis showed sharp *(02l)* and *(11l)* peaks nearby *(020)* peak, displaying perfect stacking of T–O–T layers.

A more detailed analysis of the d values and shapes of the *(001)* peaks of black talc and the other two white talc samples shows notable differences. The d_{001} value of black talc (9.435 Å) is slightly larger than that of white talc with a d_{001} value (9.410 Å). This is very similar to random chlorite/talc mixed-layers. Moreover, the full width at half maximum (FWHM) of black talc *(001)* peak is slightly larger, indicating less repetition of the T–O–T layers along the ***c*** direction or the poor crystallinity of the black talc.

3.2 Characterization of carbonaceous material (CM)

3.2.1 Raman spectroscopy

Our previous study showed that the black talc contains small amounts of organic carbon (<1.0 wt%), which causes the unusual black color (Li et al. 2013). Raman spectroscopy is an effective method for characterizing naturally occurring CM (Pasteris and Wopenka 1991; Wopenka and Padteris 1993; Jehlička et al. 1997; Beyssac et al. 2003; Quirico et al. 2005; Sadezky et al. 2005; Liu et al. 2013). Raman signals resulting from lattice vibrations of CM are highly strong, while it is weak from the mineral talc, leading to no obvious signals from the talc in the Raman spectrum of the black talc (Fig. 4).

For perfectly crystallized graphite, the Raman spectrum shows a strong sharp first-order peak at ~1582 cm^{-1} (generally termed the "G" peak or "order band") resulting from the E_{2g2} vibrational mode corresponding to in-plane vibrations of aromatic carbons in the graphitic structure with a weaker band at 42 cm^{-1} (E_{2g1}), and the second-order doublet G'_1 and G'_2 at 2695 cm^{-1} and 2735 cm^{-1}, respectively (Lespade et al. 1984; Jehlička et al. 1997; Jehlička and Beny 1999; Beyssac et al. 2002). In CM with impurities or disordered graphite structures, in addition to the G peak with some offset between 1500–1605 cm^{-1} and the G' peak at 2500–2700 cm^{-1} (resulting from the merger of the G'_1 and G'_2 peaks), a "D" peak (generally termed the "disorder band") appears at 1250–1450 cm^{-1}, induced by defects in the lattice structure, vacancies in aromatic ring lamellae, or small crystal sizes (Nemanich 1979; Bénny-Bassez and Rouzaud 1985; Yang and Wu 2008; Liu et al. 2013).

The Raman spectra of black talc acquired from different spots in individual samples and from different samples are nearly the same. A representative Raman spectrum is plotted in Fig. 4, showing a single sharp G peak at 1592 cm^{-1} (peak height = 7105.90; FWHM = 54.27 cm^{-1}) and one relatively asymmetrical broad D peak at 1329 cm^{-1} (peak height = 6012.03; FWHM = 137.34 cm^{-1}) in the first-order band region, and three broad peaks at 2593, 2872, and 3170 cm^{-1} which may be attributed to overtones of the D, G, and combined "G+D" peaks in the second-order band region, respectively (Cuesta et al. 1994; Sadezky et al. 2005).

According to Liu et al. (2013), the vitrinite reflectance (*vR*o%) of CM is related to the ratio of the G and D Raman peak height (Gh/Dh), expressed by the regression equation $vR\text{o}\% = 1.1659 \times (\text{Dh/Gh}) + 2.7588$. Based on this equation, the vitrinite reflectance of CM in the black talc is 3.76%, which is in the semi-graphite category of the International Committee for Coal and Organic Petrology (ICCP) classification scheme based on the four organic components of natural char, natural coke, semi-graphite, and graphite (Kwiecińska and Petersen 2004).

3.2.2 XPS results

The XPS spectrum of the black talc with labeled chemical states of elements for each peak (Fig. 5a) confirms the existence of Mg, Si, and O. A noticeable peak appears in the region of the C 1s binding energy interval (280–300 eV), which indicates the presence of CM in the black talc. The intensity of the C 1s peak is relatively weak compared with the Mg, Si, and O elemental peaks, because the contents of CM in the black talc are relatively low (< 1.0 wt%) (Li et al. 2013).

The XPS method reveals the binding energy of carbon atoms and distinguishes between sp^2 and sp^3 carbon bonds, and thus is a powerful tool for the structural characterization of CM, including the characterization of amorphous carbon films, and diamond-like carbon (DLC) films that contain both sp^2 and sp^3 hybridized carbon atoms (Jackson and Nuzzo 1995; Díaz et al. 1996; Merel et al. 1998; Taki and Takai 1998; Li et al. 2002; Chu and Li 2006; Park and Kim 2010). A narrow scanning spectrum (Fig. 5b) demonstrates a broad asymmetric peak, suggesting the complexity of the chemical bonds and structures constituting the CM in the black talc.

The C 1s peak was fitted by using a mixture of Gaussian and Lorentzian shape (GL(80)) after removing the linear background in the software PeakFit; the peak was decomposed into three components as shown in Fig. 5b. Here, the absolute binding energies were not rigidly fixed, as the results might be affected by sample charging; however, the binding energy shifts within the C 1s region were valid. A binding energy of 284.4 eV was adopted as the C 1s peak position characterizing sp^2 bonding (the graphite component) and the binding energy of sp^3 hybridized carbon (the diamond component) was ~ 1.0 eV higher (~285.4 eV) (Mizokawa et al. 1987; Díaz et al. 1996; Merel et al. 1998). A third peak centered at ~286.5 eV with low intensity and broad width, was added during the fitting procedure, corresponding to C–O bonds. The final fitted three peaks were: 284.4 eV (peak area = 2569.4, FWHM = 1.48 eV; sp^2 bonding), 285.2 eV (peak area =767.1, FWHM = 1.55 eV; sp^3 bonding), and 286.4 eV (peak area = 707.9, FWHM = 3.09 eV; C–O bonds). The sp^2 carbon atom content in the CM was estimated to be 63.54%, based on the ratio of the sp^2 peak area to the entire C 1s peak area. The exact proportions of sp^2, sp^3, and C–O carbon in the CM may vary randomly to a certain extent, caused by the manual fitting process, but the analysis confirms that the three types of carbon bonds are indeed present in the black talc.

3.2.3 ^{13}C isotope analysis of CM

The use of hydrous pyrolysis (with gold-tube sample capsules) to determine the ^{13}C isotope compositions of sedimentary rock samples, as applied in this study, has been shown to be highly effective in deciphering processes of gas generation, the origin of gas, and the maturation degree of organic matter (Behar et al. 1995; Cramer 2004; Kotarba and Lewan 2004; Liu et al. 2012). The ^{13}C isotopic compositions ($\delta^{13}C$) of the hydrocarbon products of hydrous pyrolysis, relative to the PDB standard (Craig 1957), show uniformly negative values between –38.82 and –34.59‰ (Table 1). Commonly, carbon isotopic compositions of CH_4 products are lighter than those of parent CM, but the fractionation effect of heavy hydrocarbon compounds (e.g., C_2H_6 and C_3H_8) is relatively weak, which can be used as an indicator of $\delta^{13}C$ values in the parent CM (Cramer 2004; Liu et al. 2012).

The average $\delta^{13}C$ value of all the alkane products in the samples was approximately –36‰, which is very close to the $\delta^{13}C$ value of organic matter in the carbonates from the Dengying Formation (–34.1‰ to –35.6‰) (Guo et al. 2007). The interpretation of organic carbon isotopic compositions in sedimentary rocks is difficult on account of the effects of post-depositional processes, which can alter primary isotopic compositions; nevertheless, the negative values still suggest that the CM in the black talc probably was derived from aquatic algae and bacteria, given the geological context of the deposits.

3.3 Direct STEM observations of CM in the black talc

Direct observations and analysis of the CM using conventional TEM is difficult, and the results depend mainly on the contents and properties of the CM in the samples. However, STEM has been proven powerful in the detection and analysis of the distribution of carbon in CM-bearing samples at nanoscales, because it provides both bright field (BF) and high-angle annular dark-field (HAADF) images in which the signal intensity is relative to the atomic number (~Z^2) and the number of atoms along the beam direction (Xu et al. 2014).

At low STEM magnification (Fig. 6a and b), BF images show apparently homogeneous structures of the black talc, while HAADF images show a certain degree of heterogeneity with some dark lines among the talc crystals, which indicates distribution and characteristics of the CM in the black talc. Magnified images (Fig. 6c and d) provide more details about these dark zones. For comparison, the simultaneously obtained BF and DF images are used to show exactly the same areas in the specimen, where the dark zones appeared in DF images give remarkable different contrasts with the surrounding talc while they are not discernable in BF images.

Monolayers of graphene-like carbon are locally observed in the talc interlayer spaces (Fig. 7). By using the d_{001} spacing of black talc obtained from XRD results (~9.4 Å) as an internal standard scale, the thickness of the thin layers was measured to be ~3.4 Å, which is equal to the thickness of monolayer graphene (Gupta et al. 2006; Nemes-Incze et al. 2008; Burnett et al. 2012) and the d_{001} spacing of graphite (~3.4 Å) (Lukesh and Pauling 1950; Wopenka and Pasteris 1993; Fayos 1999; Sadezky et al. 2005). The extra-thin layer directly contacts with two parallel T–O–T layers comfortably in the BF images.

The thicknesses of some of the dark lines were determined to be around a few nanometers (e.g., 1.37 nm and 2.31 nm in the examples in Fig. 6c), which are equal to the thicknesses of several stacked graphene-like layers. Notably, some dark zones are encompassed by talc crystals with thin lenticular-like shapes; in such situations, the CM is present as multiple layers of graphene-like carbon within the talc crystals, oriented nearly parallel to the *(001)* face of the talc crystals.

In addition, layers of graphene-like carbon were discovered at high-angle boundaries between laminar talc crystals as well (Fig. 7c and d). Stacks of carbon layers are discernable in BF images, showing typically wavy fringes of the CM (Buseck and Huang 1985; Buseck et al. 1988; Ahn et al. 1999). The thickness of single layers is ~3.4 Å, and the signal intensity under HAADF images is similar to that of monolayers of graphene-like carbon.

4. Discussion

4.1 Crystal structure of black talc

In optical microscope images (Fig. 1c and d), black talc ooids are homogeneous and yellowish, rather than colorless and transparent as in normal talc. In-situ micro-Raman spectroscopic analysis and XPS results confirm the presence of CM with both sp^2- and sp^3- hybridized carbon atoms and possible C–O or other impure bonds. The STEM images (Figs. 6 and 7) provide a direct approach for accurately measuring the thicknesses of CM layers, which are from ~3.4 Å (monolayer) to dozens of Å (multilayers) thick. The term “graphene” is used to describe a two-dimensional honeycomb lattice composed of sp^2-bonded carbon atoms with thicknesses of 3.4–3.5 Å (Soldano et al. 2010); thus, for the purposes of the present discussion, the CM in the black talc is termed as "graphene-like" carbon on account of the impurities in the bonds and defects in the crystal structure.

In general, two forms of graphene-like carbon are interstratified in talc crystals; i.e., single layers of graphene-like carbon (Fig. 7) and multiple layers of graphene-like carbon, with the *(001)* orientation of the graphene-like carbon parallel to the *(001)* orientation of the talc (Fig. 6c and d). In addition, multiple layers of graphene-like carbon also occur between laminar talc crystals (Fig. 7c and d). Similar instances of CM intergrown within phyllosilicate minerals have been discovered in illite (Ahn et al. 1999) and phlogopite (Ferraris et al. 2004). In these circumstances, the T–O–T layers or talc crystals act as protective covers that retarded the oxidation of the intergrown graphene-like carbon over prolonged periods of geological time.

Based on the proposed structural model of the black talc (Fig. 8a, b and c), more convincing interpretations of other experimental results can be approached. For example, the XRD results show that, because of the low contents and lack of periodic repetition of graphene-like carbon layers, no diffracted CM peaks appear in the XRD results; however, the d_{001} spacing of the black talc does increase slightly on account of the interstratified graphene-like carbon (Fig. 3b). Also, the existence of interlayered graphene-like carbon alters the Van der Waals bonding environment between adjacent T–O–T layers, thus disrupting the stacking order in the black talc and causing a highly asymmetrical broad peak around *(020)* and *(110)* peak positions. Meanwhile, the graphene-like carbon layers act as "slicers", which segment the talc crystals and inhibit the further growth along the ***c***-axis, resulting in a broad *(001)* peak of the black talc.

4.2 Formation of black talc

Occurrence of talc can be formed through various mechanisms within different host rocks of different ages and geological environments (Yalçin and Bozkaya 2006). The talc that forms economically important deposits are commonly generated through metamorphism of ultramafic rocks (Linder et al. 1992; Brady et al. 1998; El-Sharkawy 2000s) or hydrothermal alteration of siliceous Mg-rich carbonates (e.g., Moine et al. 1989; Hecht et al. 1999; Schandl et al. 1999; Tornos and Spiro 2000; Shin and Lee 2002; Boulvais et al. 2006), whereas sedimentary talc that form in evaporative or carbonate-rich environments are much less reported (Friedman 1965; Noack et al. 1989; Tosca et al. 2011). However, the geological background and the results of petrological, and mineralogical analyses indicate that the black talc deposits in Guangfeng were controlled by or closely related to sedimentary processes.

The Dengying Formation in Guangfeng region experienced a sedimentary environment of shallow marine or lagoon during the late Neoproterozoic era when the black talc deposits formed. Subsequently, no large-scale regional metamorphism or magmatic activities has occurred in this area (Fan 1990; Di 1993; Li 1997; Liu 2008; Lei et al. 2012), and thus the likelihood of a metamorphic or metasomatic genesis of the black talc deposits is low. In addition, the black talc ore bodies appear in stratoid shapes and conformably contact with surrounding rocks that share similar mineral assemblages, including dolomite and quartz. The occurrence of black talc layers interbedded with underlying sedimentary host rocks is occasionally observed, which indicates the black talc and surrounding rocks shared a common sedimentary environment.

The term "ooid" is used to describe spherical or subspherical grains composed of concentric layers surrounding detrital nuclei. Ooids are usually considered to form in shallow and highly agitated marine sedimentary environments or sometimes in inland lakes (Kump and Hine1986; Siewers 2003). Oolitic structures generally appear in carbonates, iron minerals, phosphates, and cherts (Simone 1980). Under certain conditions, oolites also occur in clay-rich sediments, e.g. in sediments rich in kaolinte and smectite (Sturesson et al. 1999), stevensite (Tettenhorst and Moore 1978), and talc (Noack et al. 1989). The oolitic structure is one of the most visually striking features of the black talc in Guangfeng County and probably indicates a sedimentary origin of the talc.

The paragenetic association of black talc, apatite, and pyrite in the black talc deposits is very similar to the associations observed in the talc occurrences in dolomite–quartz marbles of the Cambrian Shady Formation in eastern Alabama, where the formation of talc was interpreted to be sedimentologically controlled (Thompsn 1975). In addition, the negative ^{13}C isotopic compositions of the black talc (approximately –36‰) further suggest the existence of organic carbon originating from microorganisms. The interstratification of graphene-like carbon layers within the talc shows an extremely close relationship between the two, indicating the possible co-deposition of the talc and the organic carbon.

The precipitation of Mg-silicate minerals (e.g., sepiolite, stevensite, kerolite, and talc) in surface water environments has been extensively studied and is considered to record the primary composition of the solution of the environment in which the mineral formed (Gac et al. 1977; Tettenhorst et al. 1978; Callen 1984; Deocampo et al. 2009; Tosca et al. 2011, 2014; Bristow et al. 2012; Clauer et al. 2012). Tosca et al. (2011, 2014) made extraordinary progress and proposed that the solution required to precipitate talc at low temperatures is elevated in SiO_2 (aq), contains sufficient Mg^{2+}, has a pH of ~8.7 or above, exhibits near-marine salinities, and is lacking in soluble Al, which otherwise may facilitate precipitation of other Al-bearing clay minerals prior to talc, such as montmorillonite, chlorite, and palygorskite (Tosca et al. 2011).

The geochemical study of the black talc deposits by Lei et al. (2012) revealed that the magnesium in the black talc was mainly provided by the magnesium-rich solution in the shallow marine or lagoon environment, while the silicon was mainly derived from silicon-rich hydrothermal fluid formed by seawater infiltrating and leaching of the old crustal strata, based on the analysis of rare earth elements, the ratio of $^{87}Sr/^{86}Sr$ (0.7092 ~ 0.7101), and $\delta^{18}O_{V\text{-}SMOW}$ (14.5‰ ~ 19.7‰). The absence of Al-bearing minerals indicates an Al-depleted aquatic environment. Moreover, the close relationship between graphene-like carbon and talc indicates that organisms were probably involved in the precipitation of the Mg-silicates, which is of great importance, as organisms can affect sedimentary environment by altering the pH and oxygen fugacity of seawater, and can locally control the chemistry of pore-waters

(Tosca et al. 2011).

According to previous studies, some intermediate Mg-silicate materials with chemical compositions and structures similar to those of talc, such as sepiolite, stevensite, or kerolite, may be initially precipitated depending on the chemical conditions of the solution (e.g., pH, Mg/Si ratio, and salinity) and then be transformed into talc through dehydration and stacking ordering of Mg-silicates upon burial and heating during subsequent diagenesis (Brindley et al. 1977; Tettenhorst and Moore 1978; Noack et al. 1989; Tosca et al. 2011, 2014; Clauer et al. 2012). However, no intermediate products prior to the talc have been identified in the black talc, probably because all the intermediate materials were completely transformed into talc at some point following deposition and burial.

The formation of the black talc is complicated by the involvement of organic matter, which indicates the activity of organisms during deposition. Based on the existing genetic models of sedimentary talc formation in an oversaturated Mg^{2+}–SiO_2 (aq) system at low temperatures (Tosca et al. 2014) and combined with the presence of graphene-like carbon interstratified within the talc, a more sensible and straightforward model is proposed as below for the formation of the black talc (Fig. 8).

During the late Neoproterozoic, T–O–T layers of Mg-silicate with thicknesses of 1–2 unit cells preferentially formed and precipitated in a lagoon or shallow marine environment oversaturated with respect to Mg^{2+} and SiO_2 (aq). The thriving activities of microorganisms provided abundant organic matter for co-deposition with

Mg-silicates, through secretion or degradation of dead cells. The high surface area and layer charge resulting from impurity in T–O–T layers created an effective adsorbent for organic matter, which strengthened the bonding between Mg-silicates and organic materials. During the burial stage, the structures of the Mg-silicates and organic materials evolved synchronously due to their close relationship. The Mg-silicate layers were dehydrated and structurally reorganized in the form of increasing stacking layers (Tosca et al. 2014), while the organic materials were graphitized, which involved compositional alteration (release of O, H, N, and other elements) and structural transformation (decreasing sp^3 hybridized carbon in-plane and increasing stacking order in the ***c***-axis direction) (Buseck and Huang 1985; Wopenka and Pasteris 1993). Finally, the black talc was formed.

5. Implications

The large black talc deposits discovered in late Neoproterozoic strata located in Guangfeng County, Jiangxi Province, China, possess unique characteristics in terms of their black color, petrography, mineralogy, and sedimentary genesis. A geological survey of the district has revealed that a shallow marine or lagoon sedimentary environment was present in the Guangfeng area in the late Neoproterozoic era, and that no large-scale regional metamorphism or magmatic activity occurred in the area subsequent to this time. The connections between the black talc ores and surrounding rocks (including conformable contact relations and similar mineral compositions), indicate their analogous depositional environment. The oolitic structures and presence of organic (graphene-like) carbon, pyrite, and apatite further suggest that the formation of the black talc is controlled by or was closely related to sedimentation processes, which is rarely reported for natural talc occurrences.

The unusual black color of the Guangfeng talc is caused by contamination of the talc by poorly graphitized CM (named "graphene-like carbon" in this study), as revealed by Raman and XPS analysis. Two types of graphene-like carbon are related to the talc, as observed in STEM images: single and multiple layers of graphene-like carbon at the interlayered position of talc crystal structure, and multiple layers of graphene-like carbon at boundaries between talc crystals.

A simple model of formation is suggested for the black talc in this study with involvement of microorganisms, which provided abundant of organic matter and may have locally controlled the chemical environment, like the pH of pore waters, to facilitate talc precipitation. In this model, 2:1 Mg-silicates layers (1–2 unit cells thick) with a trioctahedral occupancy ("T–O–T"-like structure) formed preferentially and precipitated in a solution oversaturated with respect to Mg^{2+} and SiO_2 (aq). Abundant organic matter derived from the thriving microorganisms was co-deposited with the Mg-silicates. Early diagenesis promoted dehydration and structural reorganization of the Mg-silicate layers, along with graphitization of organic matter, and finally resulted in the formation of the black talc.

The precipitation of dolomite is rare in modern environments and in laboratory conditions at low temperatures, whereas it is abundant in older rocks, which brought about the "problem" on the formation mechanisms of dolomite, called "dolomite problem" (Hardie 1987; Shen et al. 2015; Zhang et al. 2012, 2015). Previous studies have shown that a key factor that inhibits dolomite formation at low temperatures is the "Mg hydration", which, however, can be weakened by adding catalysts, such as microorganisms or bound extracellular polymeric substances (EPS) (Shen et al. 2015; Zhang et al. 2015). It is likely that the conditions required for the precipitation of Mg-silicates are analogous to those for the precipitation of Mg-carbonates. In this study, a close relationship between Mg-silicates and organic matter is conspicuous, given that the graphene-like carbon is interstratified within the talc. It is therefore possible that the microorganisms and EPS played an important role in facilitating the precipitation of Mg-silicates. However, the exact role of microoganisms and EPS in black talc formation, and details of the precipitation mechanism remain unclear and thus require further investigation. Our study may also help us to better understand recently discovered deep-water hydrocarbon reservoirs related to pre-salt lacustrine layers with talc and dolomite.

Clay minerals reacting with different types of organic compounds are common in nature and in the laboratory, especially involving the T–O–T type clay minerals such as montmorillonite (Bergaya and Lagaly 2013). The black talc of the present study can be treated as a natural organic–clay material that may have potential industrial applications based on the interstratification of the graphene-like carbon within the talc. Although the content of organic carbon in the black talc is not high (<1 wt%), the total amount preserved in the black talc deposits is still significant, and may have contributed to the global carbon cycle during the late Neoproterozoic, considering the large reserves, stabilized relationship between carbon and talc, and more discoveries of black talc (or organic carbon-bearing talc) in southern China and worldwide.

Acknowledgments

The authors appreciate the financial support from the National Natural Science Foundation of China (Grant Nos. 41472033 and 41425009), and the NASA Astrobiology Institute (N07-5489). The first author thanks the China Scholarship Council (CSC) for providing funding to support the Joint Education Program.

References

Ahn, J.H., Cho, M., and Buseck, P.B. (1999) Interstratification of carbonaceous material within illite. American Mineralogist, 84, 1967-1970.

Behar, F., Vandenbroucke, M., Teermann, S. C., Hatcher, P. G., Leblond, C., and Lerat, O. (1995) Experimental simulation of gas generation from coals and a marine kerogen. Chemical Geology, 126(3), 247-260.

Bergaya, F., and Lagaly, G. (2013) Handbook of clay science (Vol. 5). Newnes, chapter 2 and chapter 10.Bénny-Bassez, C., and Rouzaud, J. N. (1985) Characterization of carbonaceous materials by correlated electron and optical microscopy and Raman microspectrometry. Scanning Electron Microscopy, 1, 119-132.

Beyssac, O., Goffé, B., Chopin, C., and Rouzaud, J. N. (2002) Raman spectra of carbonaceous material in metasediments: a new geothermometer. Journal of metamorphic Geology, 20(9), 859-871.

Beyssac, O., Goffé, B., Petitet, J. P., Froigneux, E., Moreau, M., and Rouzaud, J. N. (2003) On the characterization of disordered and heterogeneous carbonaceous materials by Raman spectroscopy. Spectrochimica Acta Part A: Molecular and Biomolecular Spectroscopy, 59(10), 2267-2276.

Boulvais, P., De Parseval, P., D'Hulst, A., and Paris, P. (2006) Carbonate alteration associated with talc-chlorite mineralization in the eastern Pyrenees, with emphasis on the St. Barthelemy Massif. Mineralogy and Petrology, 88(3-4), 499-526.

Brady, J. B., Cheney, J. T., Rhodes, A. L., Vasquez, A., Green, C., Duvall, M. and Kovaric, D. (1998) Isotope geochemistry of Proterozoic talc occurrences in Archean marbles of the Ruby Mountains, southwest Montana, USA. Geol Mater Res, 1, 1-41.

Brindley, G. W., Bish, D. L., and Wan, H. M. (1977) The nature of kerolite, its relation to talc and stevensite. Mineralogical Magazine, 41(320), 443-452.

Bristow, T. F., Kennedy, M. J., Morrison, K. D., and Mrofka, D. D. (2012) The influence of authigenic clay formation on the mineralogy and stable isotopic record of lacustrine carbonates. Geochimica et Cosmochimica Acta, 90, 64-82.

Burnett, T. L., Yakimova, R., and Kazakova, O. (2012) Identification of epitaxial graphene domains and adsorbed species in ambient conditions using quantified topography measurements. Journal of Applied Physics, 112(5), 054308

Buseck, P. R. and Huang, B.J. (1985) Conversion of carbonaceous material to graphite during metamorphism. Geochimica et Cosmochimica Acta, 49, 2003–2016.

Buseck, P. R., Huang, B. J., and Miner, B. (1988) Structural order and disorder in Precambrian kerogens. Organic Geochemistry, 12, 221–234.

Callen, R. A. (1984) Clays of the palygorskite-sepiolite group: depositional environment, age and distribution. Developments in Sedimentology, 37, 1-37.

Chu, P. K., and Li, L. (2006) Characterization of amorphous and nanocrystalline carbon films. Materials Chemistry and Physics, 96(2), 253-277.

Clauer, N., Fallick, A. E., Galán, E., Pozo, M., and Taylor, C. (2012) Varied crystallization conditions for Neogene sepiolite and associated Mg-clays from Madrid Basin (Spain) traced by oxygen and hydrogen isotope geochemistry. Geochimica et Cosmochimica Acta, 94, 181-198.

Craig, H. (1957) Isotopic standards for carbon and oxygen and correction factors for mass-spectrometric analysis of carbon dioxide. Geochimica et cosmochimica acta, 12(1), 133-149.

Cramer, B. (2004) Methane generation from coal during open system pyrolysis investigated by isotope specific, Gaussian distributed reaction kinetics. Organic Geochemistry, 35(4), 379-392.

Cuesta, A., Dhamelincourt, P., Laureyns, J., Martinez-Alonso, A., and Tascón, J. D. (1994) Raman microprobe studies on carbon materials. Carbon, 32(8), 1523-1532.

Deocampo, D. M., Cuadros, J., Wing-Dudek, T., Olives, J., and Amouric, M. (2009) Saline lake diagenesis as revealed by coupled mineralogy and geochemistry of multiple ultrafine clay phases: Pliocene Olduvai Gorge, Tanzania. American Journal of Science, 309(9), 834-868.

Di, S. (1993) Geological characteristics of sedimentary black talc deposits of Sinian in Pingtang, Guangfeng (in Chinese). China Non-Metallic Mining Industry Herald, 65, 11-20.

Díaz, J., Paolicelli, G., Ferrer, S., and Comin, F. (1996) Separation of the sp 3 and sp 2 components in the C1s photoemission spectra of amorphous carbon films. Physical Review B, 54(11), 8064.

El-Sharkawy, M. F. (2000) Talc mineralization of ultramafic affinity in the Eastern Desert of Egypt. Mineralium Deposita, 35(4), 346-363.

Fan, M. (1990) Geological characteristics of black talc ores in Xitan, Guangfeng area, Jiangxi province (in Chinese). Non-Metallic Mines, 4, 1-3.

Fayos, J. (1999) Possible 3D carbon structures as progressive intermediates in graphite to diamond phase transition. Journal of Solid State Chemistry, 148(2), 278-285.

Ferraris, C., Grobety, B., Früh-Green, G.L., and Wessicken, R. (2004) Intergrowth of graphite within phlogopite from Finero ultramafic complex (Italian Western Alps): implications for mantle crystallization of primary-texture mica. European Journal of Mineralogy, 16, 899-908.

Friedman, G.M. (1965) Occurrence of talc as a clay mineral in sedimentary rocks. Nature, 207, 283-284.

Gac, J. Y., Droubi, A., Fritz, B., and Tardy, Y. (1977) Geochemical behaviour of silica and magnesium during the evaporation of waters in Chad. Chemical Geology, 19(1), 215-228.

Guo, Q., Strauss, H., Liu, C., Goldberg, T., Zhu, M., Pi, D., and Fu, P. (2007) Carbon isotopic evolution of the terminal Neoproterozoic and early Cambrian: evidence from the Yangtze Platform, South China. Palaeogeography, Palaeoclimatology, Palaeoecology, 254(1), 140-157.

Gupta, A., Chen, G., Joshi, P., Tadigadapa, S., and Eklund, P. C. (2006) Raman scattering from high-frequency phonons in supported n-graphene layer films. Nano letters, 6(12), 2667-2673.

Hardie, L. A. (1987) Dolomitization-a critical view of some current views. Journal of Sedimentary Research, 57(1), 166-183.

Hecht, L., Freiberger, R., Gilg, H. A., Grundmann, G., and Kostitsyn, Y. A. (1999) Rare earth element and isotope (C, O, Sr) characteristics of hydrothermal carbonates: genetic implications for dolomite-hosted talc mineralization at Göpfersgrün (Fichtelgebirge, Germany). Chemical Geology, 155(1), 115-130.

Jackson, S. T., and Nuzzo, R. G. (1995) Determining hybridization differences for amorphous carbon from the XPS C 1s envelope. Applied Surface Science, 90(2), 195-203.

Jehlička, J., Bény, C., and Rouzaud, J. N. (1997) Raman microspectrometry of accumulated non□graphitized solid bitumens. Journal of Raman spectroscopy, 28(9), 717-724.

Jehlička, J., and Beny, C. (1999) First and second order Raman spectra of natural highly carbonified organic compounds from metamorphic rocks. Journal of molecular structure, 480, 541-545.

Kirkland, E.J. (1998) Advanced Computing in Electron Microscopy. Plenum Press, New York.

Kotarba, M. J., and Lewan, M. D. (2004) Characterizing thermogenic coalbed gas from Polish coals of different ranks by hydrous pyrolysis. Organic Geochemistry, 35(5), 615-646.

Kump, L. R., and Hine, A. C. (1986) Ooids as sea-level indicators. In Sea-Level Research, Springer Netherlands, 175-193.

Kwiecińska, B., and Petersen, H. I. (2004) Graphite, semi-graphite, natural coke, and natural char classification—ICCP system. International Journal of Coal Geology, 57(2), 99-116.

Lei, H., Jiang, S., Sun, Y., Luo, P., Li, Y., and Ma, Z. (2012) Genesis of Yangcun superlarge talc deposit in Guangfeng, Jiangxi Province (in Chinese). Mineral Deposits, 31(2), 241-254;

Lespade, P., Marchand, A., Couzi, M., and Cruege, F. (1984) Caracterisation de materiaux carbones par microspectrometrie Raman. Carbon, 22(4), 375-385.

Li, C., Wang, R., Lu, X., and Zhang, M. (2013) Mineralogical characteristics of unusual black talc ores in Guangfeng County, Jiangxi Province, China. Applied Clay Science, 74, 37-46.

Li, L., Zhang, H., Zhang, Y., Chu, P. K., Tian, X., Xia, L., and Ma, X. (2002) Structural analysis of arc deposited diamond-like carbon films by Raman and X-ray photoelectron spectroscopy. Materials Science and Engineering: B, 94(1), 95-101.

Li, X. (1997) The Sinian lithostratigraphic framework in Dexing- Guangfeng area, Jiangxi (in Chinese). Jiangxi Geology, 11(3), 39-45.

Liu, T. (2008) Stratigraphy (lithostratic) of Jiangxi Province. China University of Geosciences Press, 147~151.

Linder, D. E., Wylie, A. G., and Candela, P. A. (1992) Mineralogy and origin of the State Line talc deposit, Pennsylvania. Economic Geology, 87(6), 1607-1615

Ling, H. F., Chen, X., Li, D., Wang, D., Shields-Zhou, G. A., and Zhu, M. (2013) Cerium anomaly variations in Ediacaran–earliest Cambrian carbonates from the Yangtze Gorges area, South China: implications for oxygenation of coeval shallow seawater. Precambrian Research, 225, 110-127.

Liu, D., Xiao, X., Tian, H., Min, Y., Zhou, Q., Cheng, P., and Shen, J. (2013) Sample maturation calculated using Raman spectroscopic parameters for solid organics: Methodology and geological applications. Chinese Science Bulletin, 58(11), 1285-1298.

Liu, W., Wang, J., Qin, J., and Zheng, L. (2012) Stable carbon isotopes of gaseous alkanes as genetic indicators inferred from laboratory pyrolysis experiments of various marine hydrocarbon source materials from southern China. Science China Earth Sciences, 55(6), 966-974.

Lukesh, J. S., and Pauling, L. (1950) The problem of the graphite structure. American Mineralogist, 35(1-2), 125.

Merel, P., Tabbal, M., Chaker, M., Moisa, S., and Margot, J. (1998) Direct evaluation of the sp 3 content in diamond-like-carbon films by XPS. Applied Surface Science, 136(1), 105-110.

Mizokawa, Y., Miyasato, T., Nakamura, S., Geib, K. M., and Wilmsen, C. W. (1987) The C KLL first-derivative x-ray photoelectron spectroscopy spectra as a fingerprint of the carbon state and the characterization of diamondlike carbon films. Journal of Vacuum Science & Technology A, 5(5), 2809-2813.

Moine, B., Fortune, J. P., Moreau, P., and Viguier, F. (1989) Comparative mineralogy, geochemistry, and conditions of formation of two metasomatic talc and chlorite deposits; Trimouns (Pyrenees, France) and Rabenwald (Eastern Alps, Austria). Economic Geology, 84(5), 1398-1416.

Nellist, D.P. (2007) Scanning transmission electron microscopy. Science of Microscopy, I, 65–132.

Nemanich, R. J., and Solin, S. A. (1979) First-and second-order Raman scattering from finite-size crystals of graphite. Physical Review B, 20(2), 392.

Nemes-Incze, P., Osváth, Z., Kamarás, K., and Biró, L. P. (2008) Anomalies in thickness measurements of graphene and few layer graphite crystals by tapping mode atomic force microscopy. Carbon, 46(11), 1435-1442.

Noack, Y., Decarreau, A., Boudzoumou, F., and Trompette, R. (1989) Low-temperature oolitic talc in upper Proterozoic rocks, Congo. Journal of Sedimentary Research, 59(5).

Park, S. J., and Kim, K. S. (2010) Surface characterization of carbon materials by X-ray photoelectron spectroscopy. Mendez-Vilas A, Diaz J. Microscopy: Science, Technology, Applications and Education. Formatex, 1905-16.

Pasteris, J.D., and Wopenka, B. (1991) Raman spectra of graphite as indicators of degree of metamorphism. Canadian Mineralogist, 29, 1-9.

Quirico, E., Rouzaud, J. N., Bonal, L., and Montagnac, G. (2005) Maturation grade of coals as revealed by Raman spectroscopy: Progress and problems. Spectrochimica Acta Part A: Molecular and Biomolecular Spectroscopy, 61(10), 2368-2377.

Rayner, J. H. and Brown G. (1973) The crystal structure of talc. Clays and Clay Minerals, 21, 103-114.

Sadezky, A., Muckenhuber, H., Grothe, H., Niessner, R., and Pöschl, U. (2005) Raman microspectroscopy of soot and related carbonaceous materials: spectral analysis and structural information. Carbon, 43(8), 1731-1742.

Schandl, E.S., Sharara, N.A. and Gorton, M.P. (1999) The origin of the Atshan talc deposit in the Hamata area, eastern desert, Egypt: a geochemical and mineralogical study. The Canadian Mineralogist, 37, 1211-1227.

Shen, Z., Brown, P. E., Szlufarska, I., and Xu, H. (2015) Investigation of the role of polysaccharide in the dolomite growth at low temperature by using atomistic simulations. Langmuir, 31, 10435-10442.

Shin, D., and Lee, I. (2002) Carbonate-hosted talc deposits in the contact aureole of an igneous intrusion (Hwanggangri mineralized zone, South Korea): geochemistry, phase relationships, and stable isotope studies. Ore Geology Reviews, 22(1), 17-39.

Siewers, F. D. (2003) Oolite and coated grains. In Sedimentology, Springer Netherlands, 814-820.

Simone, L. (1980) Ooids: a review. Earth-Science Reviews, 16, 319-355.

Soldano, C., Mahmood, A., and Dujardin, E. (2010) Production, properties and potential of graphene. Carbon, 48(8), 2127-2150.

Sturesson, U., Dronov, A., and Saadre, T. (1999) Lower Ordovician iron ooids and associated oolitic clays in Russia and Estonia: a clue to the origin of iron oolites?. Sedimentary Geology, 123(1), 63-80.

Taki, Y., and Takai, O. (1998). XPS structural characterization of hydrogenated amorphous carbon thin films prepared by shielded arc ion plating. Thin Solid Films, 316(1), 45-50.

Tettenhorst, R., and Moore Jr, G. E. (1978) Stevensite oolites from the Green River Formation of central Utah. Journal of Sedimentary Research, 48(2).

Thompsn, A. M. (1975) Talc paragenesis in some siliceous dolomitic rocks, and its sedimentologic significance. Contributions to Mineralogy and Petrology, 52(2), 133-142.

Tornos, F., and Spiro, B. F. (2000) The geology and isotope geochemistry of the talc deposits of Puebla de Lillo (Cantabrian Zone, Northern Spain). Economic Geology, 95(6), 1277-1296.

Tosca, N. J., Macdonald, F. A., Strauss, J. V., Johnston, D. T., and Knoll, A. H. (2011) Sedimentary talc in Neoproterozoic carbonate successions. Earth and Planetary Science Letters, 306(1), 11-22.

Tosca, N. J., and Masterson, A. L. (2014) Chemical controls on incipient Mg-silicate crystallization at 25° C: Implications for early and late diagenesis. Clay Minerals, 49(2), 165-194.

Wopenka, B., and Pasteris, J.D. (1993) Structural characterization of kerogens to granulite-facies graphite: Applicability of Raman microprobe spectroscopy. American Mineralogist, 78, 533-557.

Xu, H., Shen, Z., Konishi, H., and Luo, G. (2014) Crystal structure of Guinier-Preston zones in orthopyroxene: Z-contrast imaging and ab inito study. American Mineralogist, 99, 2043-2048.

Yalçin, H., and Bozkaya, Ö. (2006) Mineralogy and geochemistry of Paleocene ultramafic-and sedimentary-hosted talc deposits in the southern part of the Sivas Basin, Turkey. Clays and Clay Minerals, 54(3), 333-350.

Yang, X., and Wu, Q. (2008) Raman Spectroscopy Analysis and Application (in Chinese). Beijing: National Defense Industry Press, 210–243.

Zhang, F., Xu, H., Konishi, H., Roden, E. E. (2015) The catalysis effect of bound extracellular polymeric substances excreted by anaerobic microorganisms on Ca-Mg carbonate precipitation: Implications for the “dolomite problem.” American Mineralogist, 100, 483–494.

Zhang, F., Xu, H., Konishi, H., Shelobolina, E. S., and Roden, E. E. (2012) Polysaccharide-catalyzed nucleation and growth of disordered dolomite: A potential precursor of sedimentary dolomite. American Mineralogist, 97, 556-567.

Zhang, S., Mi, J., He, K. (2013) Synthesis of hydrocarbon gases from four different carbon sources and hydrogen gas using a gold-tube system by Fisher-Tropsch method. Chemical Geology, 349-350, 27-35.

Figure captions

FIGURE 1. **(a)** Field photographs of black talc ores. Areas enclosed by white dashed lines are layers of oolitic black talc ore. **(b)** Enlargemwnt of the oolitic black talc ores. Black spherical particles are composed of pure black talc and occur in dolomite and quartz. **(c)** Photomicrograph of an oolite-bearing sample (plane-polarized light). **(d)** Photomicrograph of an oolite-bearing sample (cross-polarized light).

FIGURE 2. SEM **(a, b, c)** and TEM **(d)** images of black talc crystals. **(a)** and **(b)** Tiny flakes of talc crystals. **(c)** Micro-sized aggregates of talc crystals surrounded by talc flakes. **(d)** HRTEM image showing the layered structure of talc crystals with thin thicknesses. **(e)** FFT patterns of the lamellar area in (d).

FIGURE 3. **(a)** XRD patterns of black talc and white talc samples. WT-1: aggregates of fine white talc crystals from Trimouns, France; WT-2: Well-crystallized monocrystal of talc. **(b)** Enlargement of the 001 peak showing differences in the d_{001} spacing and peak widths.

FIGURE 4. Raman spectrum of black talc.

FIGURE 5. XPS spectrum of black talc **(a)** and enlargement of the scanning area of C 1s (from 280 to 300 eV) **(b)**.

FIGURE 6. Bright-field (BF) (**a** and **c**) and dark-field (DF) (**b** and **d**) STEM images of black talc crystals.

FIGURE 7. Bright-field (BF) (**a** and **c**) and dark-field (DF) (**b** and **d**) STEM images of black talc crystals.

FIGURE 8. Schematic diagrams of the structures (**a**–**d**) and formation mechanisms

(**1**–**3**) of black talc. **(1)** In a shallow marine environment saturated with respect to Mg^{2+} and SiO_2 (aq), 2:1 layers of Mg-silicates precipitate along with microorganisms and organic compounds. **(2)** The precipitates, which are mixtures of Mg-silicate layers and organic carbonaceous material, initially take the shape of ooids. **(3)** The ooids are buried and diagenesis facilitates the formation of black talc. **(a)** and **(b)**: Monolayer and multilayers of graphene-like carbon in the interlayer positions of the talc crystal structure. **(c)** Multilayers of graphene-like carbon at high-angle boundaries of talc crystals. **(d)** Simplified structural diagram of graphene-like carbon (C-black balls) with defects and heteroatoms (O-red balls, N-blue balls, H-grey balls).

Table 2. Carbon isotopic compositions of alkane products of carbonaceous materials in black talc ores through hydrous pyrolysis treatment.

Sample	$\delta^{13}CH_4$ (‰)	$\delta^{13}C_2H_6$ (‰)	$\delta^{13}C_3H_8$ (‰)	$\delta^{13}C_4$ (‰)	$\delta^{13}C_5$(‰)
GF-7 +H_2O	-36.397	-37.299	-36.755	-36.146	-
GF-12 +H_2O	-37.081	-35.644	-35.234	-36.502	-36.07
Ooids+H_2O	-37.885	-35.478	-34.586	-38.823	-

Experiment conditions: Temperature: 400 °C; Time: 5 days; Pressure: 25 Mpa.

“-” no detection

Figure 1

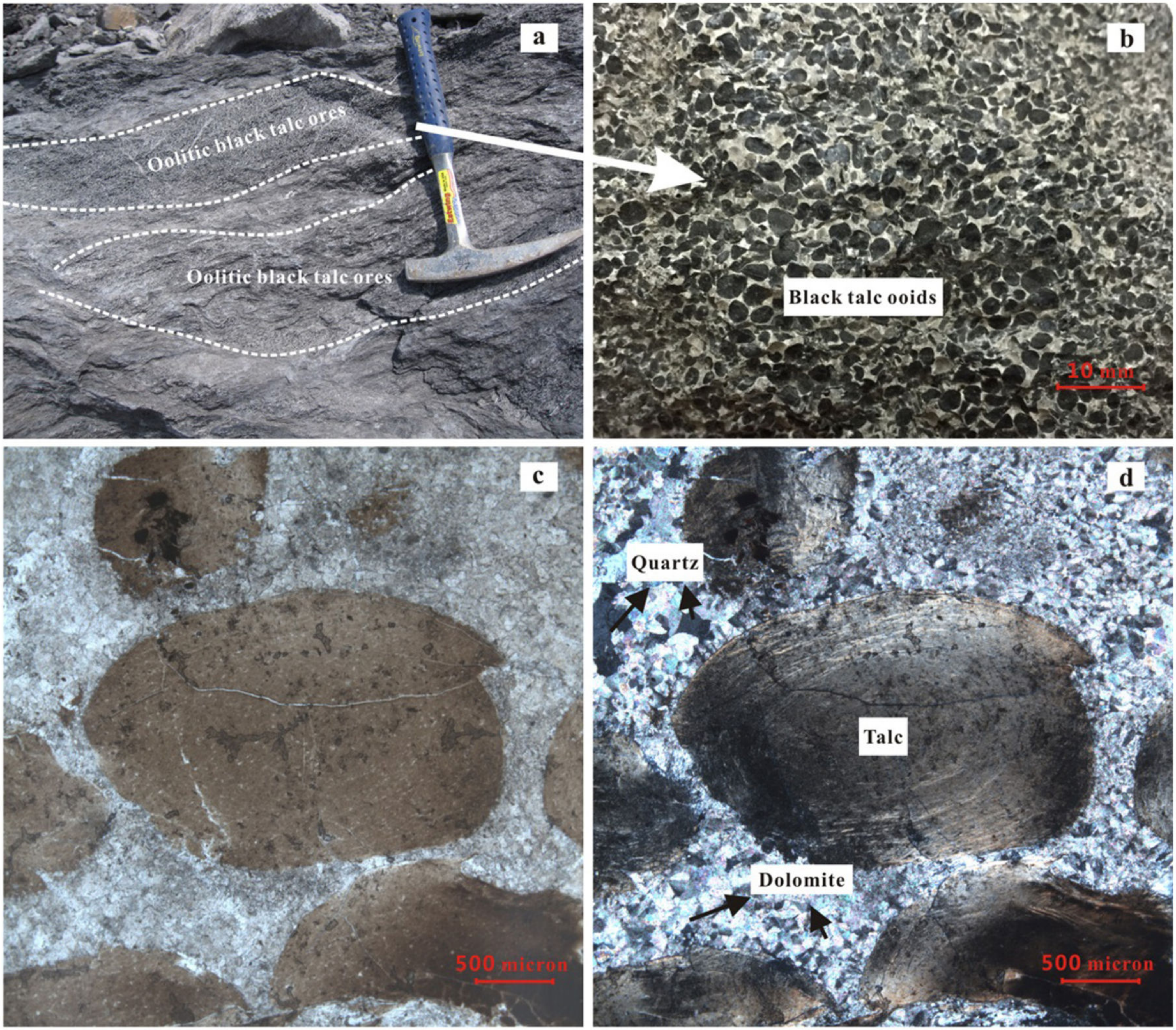
a
Oolitic black talc ores
Oolitic black talc ores
b
Black talc ooids
10 mm
c
500 micron
d
Quartz
Talc
Dolomite
500 micron

Figure 2

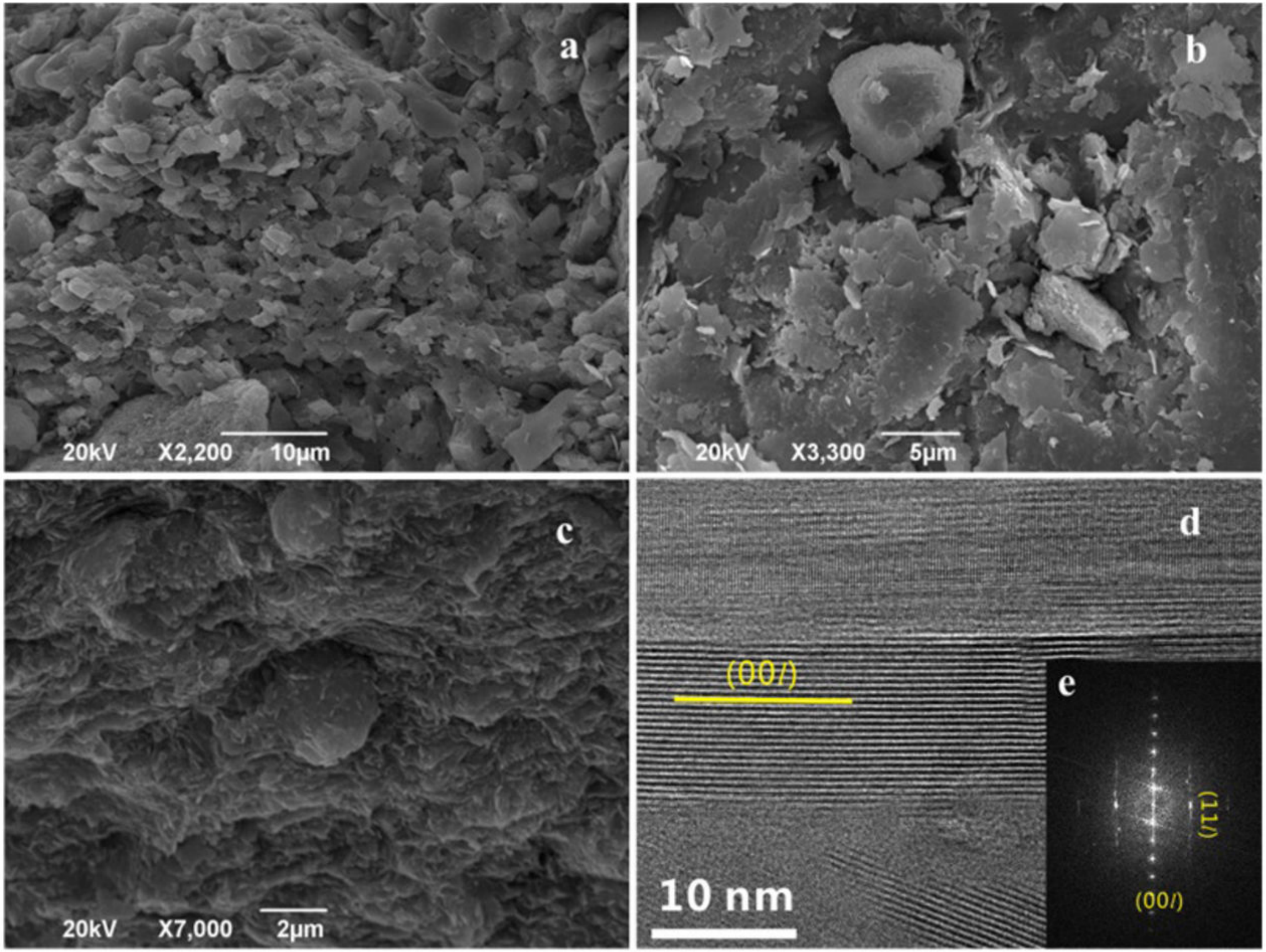
a
20kV X2,200 10μm
b
20kV X3,300 5μm
c
20kV X7,000 2μm
d
(00*l*)
e
(11*l*)
(00*l*)
10 nm

Figure 3

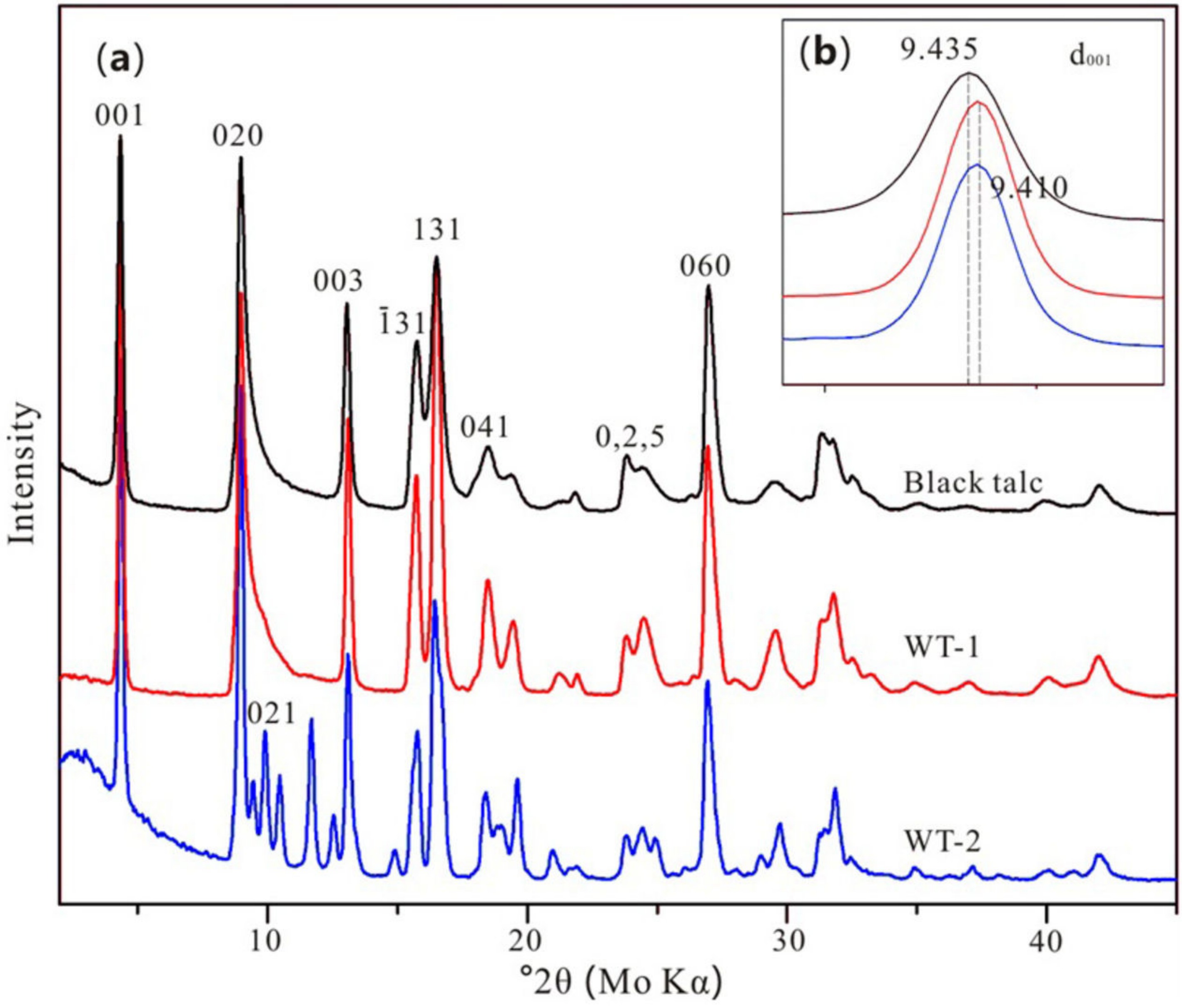
(a)
001
020
003
$\bar{1}$31
131
041
0,2,5
060
021
Black talc
WT-1
WT-2
Intensity
10
20
30
40
°2θ (Mo Kα)
(b)
9.435
d001
9.410

Figure 4

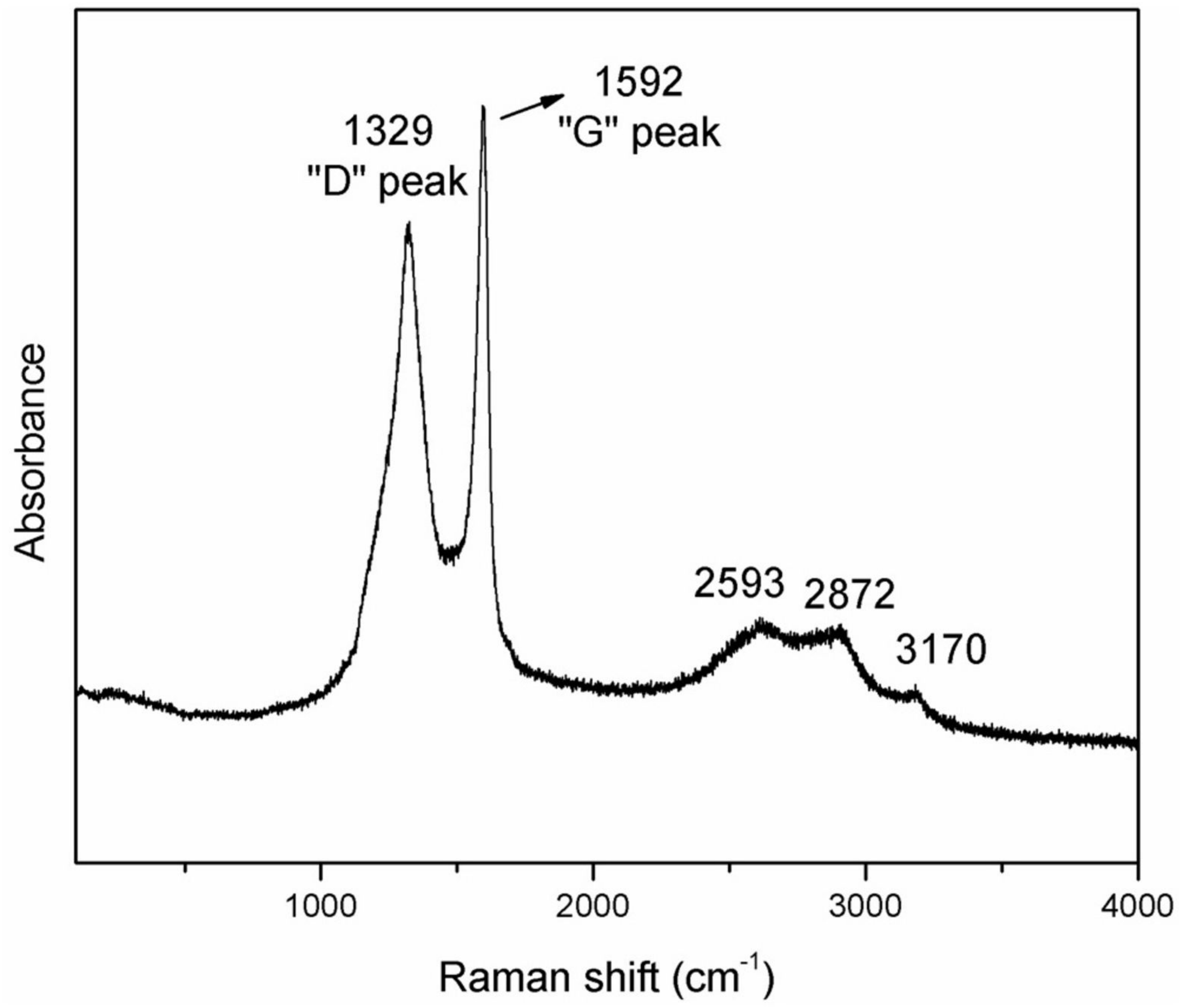
1592
"G" peak
1329
"D" peak
2593
2872
3170
Absorbance
1000
2000
3000
4000
Raman shift (cm^{-1})

Figure 5

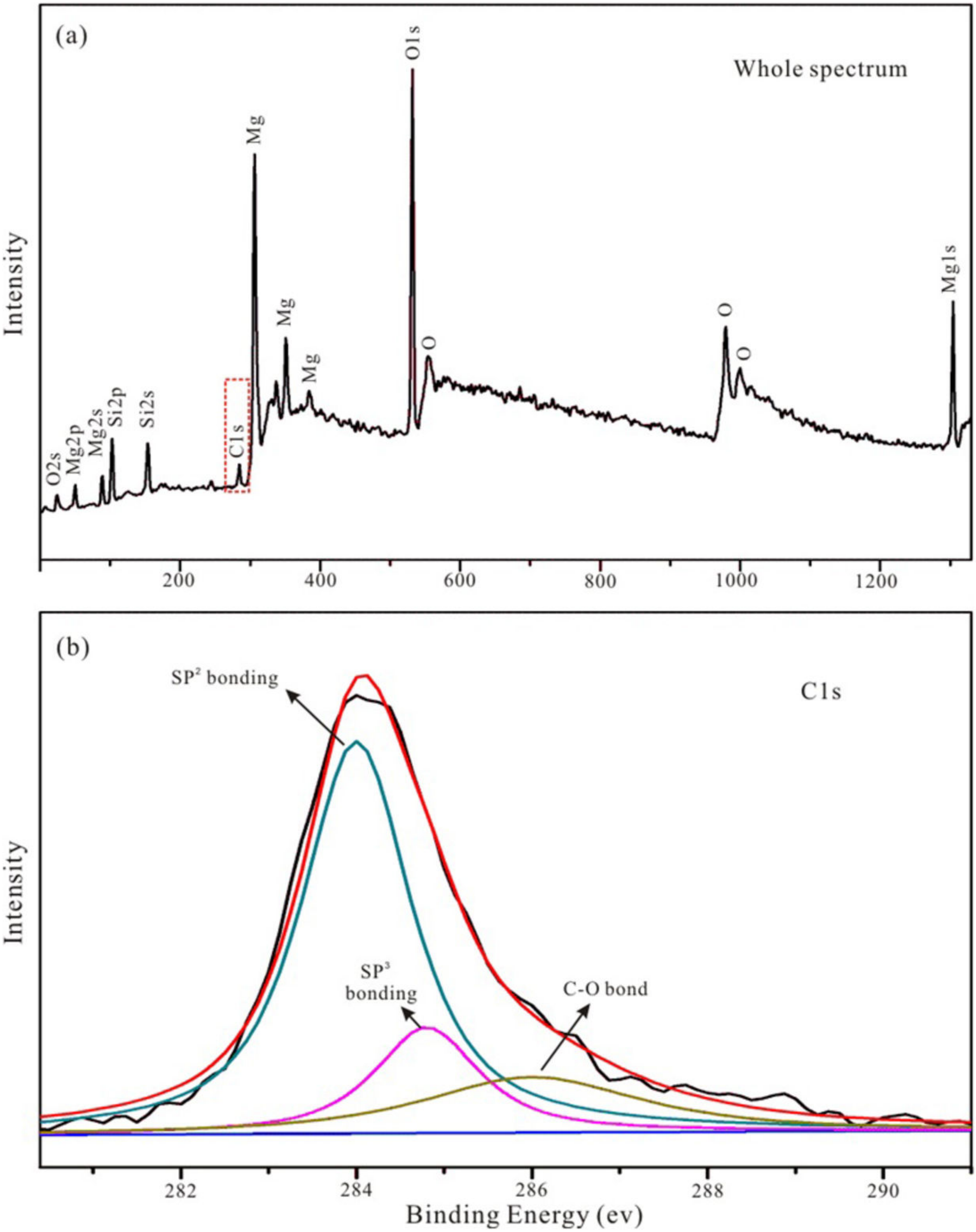
(a)
Whole spectrum
Intensity
O2s
Mg2p
Mg2s
Si2p
Si2s
C1s
Mg
Mg
Mg
O1s
O
O
O
Mg1s
200
400
600
800
1000
1200
(b)
C1s
SP^2 bonding
SP^3 bonding
C-O bond
Intensity
282
284
286
288
290
Binding Energy (ev)

Figure 6

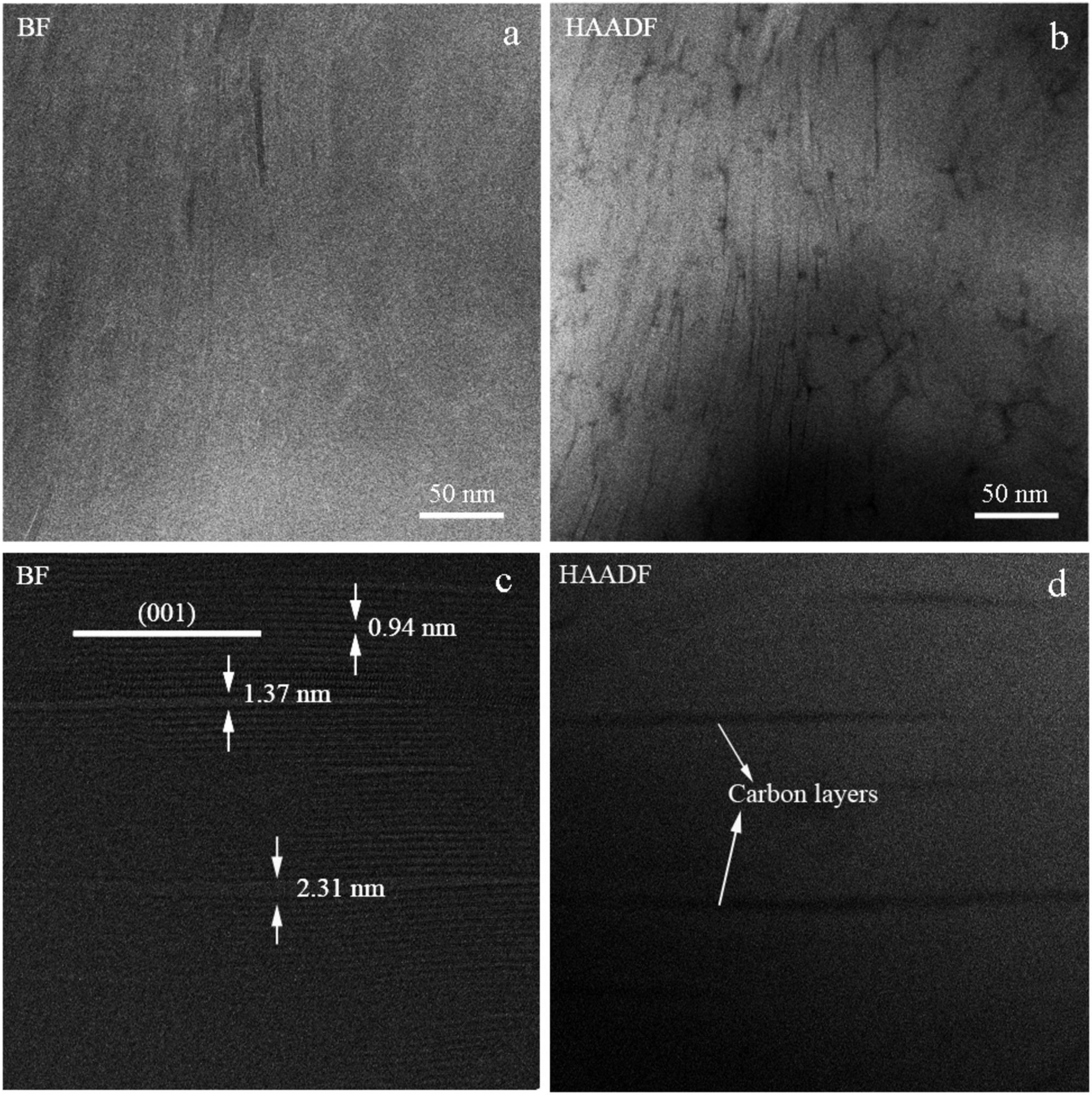
BF
a
50 nm
HAADF
b
50 nm
BF
c
(001)
0.94 nm
1.37 nm
2.31 nm
HAADF
d
Carbon layers

Figure 7

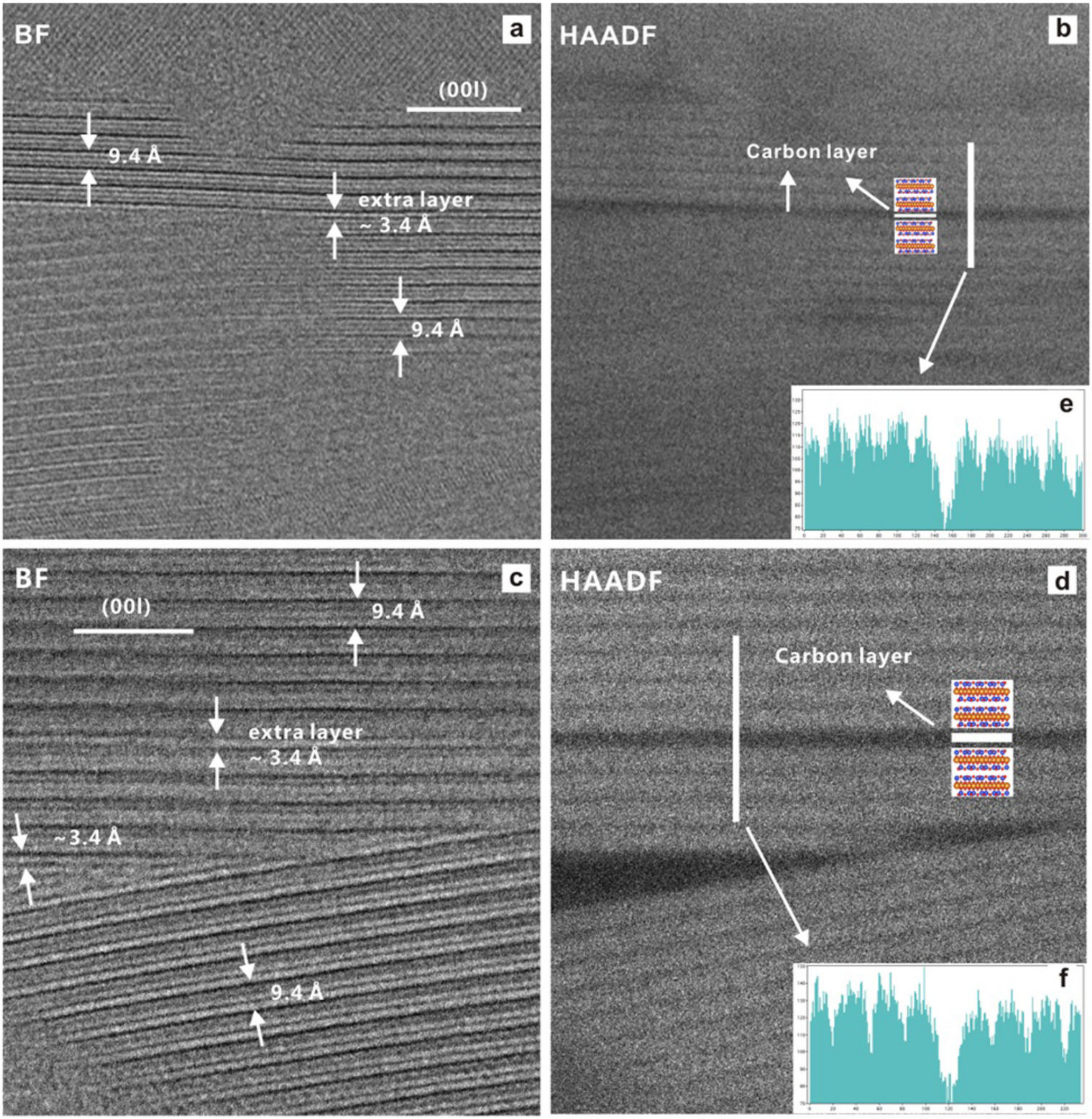
BF
a
(00l)
9.4 Å
extra layer
~ 3.4 Å
9.4 Å
HAADF
b
Carbon layer
e
BF
c
(00l)
9.4 Å
extra layer
~ 3.4 Å
~3.4 Å
9.4 Å
HAADF
d
Carbon layer
f

Figure 8

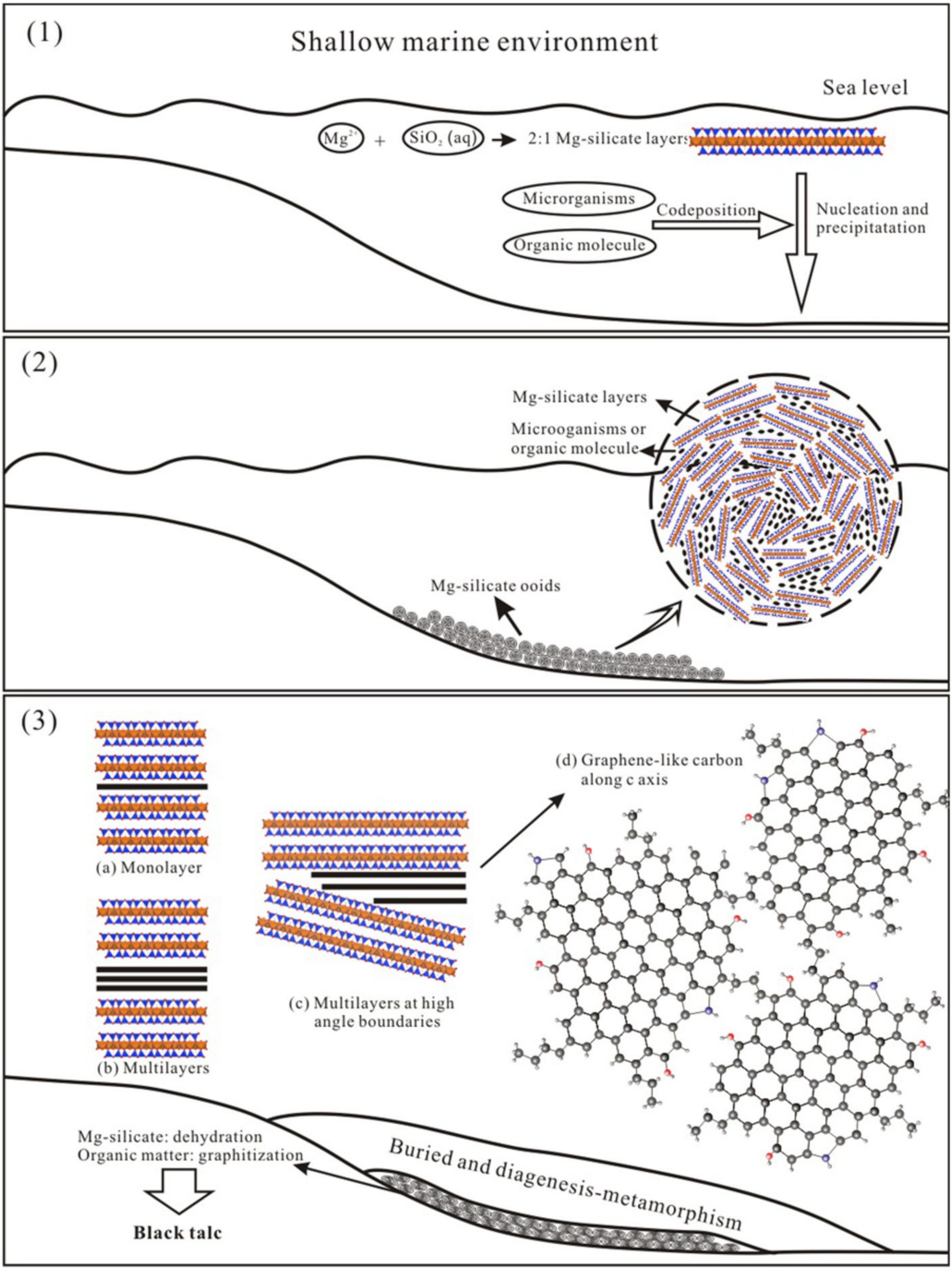
(1)
Shallow marine environment
Sea level
Mg^{2+} + SiO_2 (aq) → 2:1 Mg-silicate layers
Microrganisms
Organic molecule
Codeposition
Nucleation and precipitatation
(2)
Mg-silicate layers
Microoganisms or organic molecule
Mg-silicate ooids
(3)
(a) Monolayer
(b) Multilayers
(c) Multilayers at high angle boundaries
(d) Graphene-like carbon along c axis
Mg-silicate: dehydration
Organic matter: graphitization
Black talc
Buried and diagenesis-metamorphism